Nigerian Journal of Physics (NJP)
ISSN online: 3027-0936
ISSN print: 1595-0611
DOI: https://doi.org/10.62292/njp.v34i2.2025.393
Volume 34(2), June 2025

Influence of Gas Flow Rate on the Properties of In_2O_3 Nanostructures Synthesized on Ni/Si Substrates using a Carbothermal Reduction Process at Atmospheric Pressure

*[1]Aper, T. M., [1]Ikyumbur, J. T., [2,3]McAsule, A. A., [3,4]Obaseki, O. S. and [1]Tyona, M. D.

[1]Department of Physics, Rev.Fr. Moses Orshio Adasu University, P. M. B. 102119, Makurdi, Nigeria
[2]Department of Industrial Physics, Joseph Sarwuan Tarka University, P.M.B. 2373 Makurdi, Nigeria
[3]School of Physics, Universiti Sains Malaysia, 11800 Penang, Malaysia
[4]Department of Physical Sciences, Landmark University, PMB 1001 Omu-Aran, Kwara State, Nigeria

*Corresponding author's email: taper@bsum.edu.ng

Keywords:
Indium oxide nanostructures,
Carbothermal reduction,
Atmospheric pressure,
Crystallite size,
Optical bandgap.

ABSTRACT

Indium oxide nanostructured films have been grown on Ni/Si substrates by a carbothermal reduction of In_2O_3 powder under the flow of a 1 % hydrogen balance nitrogen as carrier gas at atmospheric pressure. The properties of the microstructures were investigated by varying the gas flow rates between 100 and 250 sccm. The films' morphological, structural and optical properties were examined using field emission scanning electron microscope (FESEM), X-ray diffraction (XRD), and UV-vis measurements. Investigation of the crystal structures revealed clear diffraction peaks in the XRD analysis corresponding to the body-centred crystal structure of the In_2O_3. The shape, crystallite size, and optical bandgap were observed to be influenced by the variation in the gas flow rates.

INTRODUCTION

Indium oxide is an important metal oxide semiconductor material with n-type conductivity. It is known to have a wide bandgap in the range of ≈3.0-3.75 ev (Chong et al., 2013; King et al., 2009), high transparency in the visible region and high reflectivity in the infrared region (Bel et al., 1998), good chemical stability, and low resistivity (Chen et al., 2020; Her & Chang, 2017). These unique properties have made it attractive for many scientific and technological device applications such as biological sensors (Qurashi et al., 2010), photovoltaic application (Abdulkadir et al., 2020), optoelectronic devices, including; heat-reflecting mirrors, flat panel display devices (Elam et al., 2006), photocatalysis (Hoch et al., 2016), gas sensors (Makhija et al., 2005), etc.

Doped and un-doped In_2O_3 films have been synthesized by different techniques such as spray pyrolysis (Prathap et al., 2005), sol-gel spin coating (Hosseini et al., 2013), sputtering (Ahmed et al., 2019), thermal evaporation (Cho et al., 2000; Hassanien & Akl, 2016), chemical vapour deposition (CVD) (Tuzluca et al., 2018), and so on. Among the deposition techniques, the CVD offers a convenient method for fabricating high-yield In_2O_3 films with good crystallinity and high purity. Because of the associated vacuum, near-vacuum, or low oxygen partial pressure growth ambient, CVD synthesized films are usually deficient in oxygen and have better conductivity than the homogenous stoichiometric In_2O_3 films. Using the CVD growth process, In_2O_3 films of varying physical properties have been synthesized by manipulating several experimental conditions such as; temperature, precursor material, carrier gas, growth ambient, etc. Carrier gas flow rates have been reported to influence the morphology of In_2O_3 films (Karn et al., 2017) greatly. Whereas argon (Ar) gas has been commonly used as a carrier in the CVD synthesis of In_2O_3 films, there has been no report on investigating other gases such as 1 % H_2 balance N_2 gas as carrier gas in the synthesis of In_2O_3 films.

In this work, we report the synthesis of In_2O_3 nanostructured films using the CVD growth technique through a carbothermal reduction of In_2O_3 powder at atmospheric pressure. A 1 % hydrogen balance nitrogen gas is employed as the carrier gas. The influence of carrier gas on the microstructures is investigated at various gas flow rates.

MATERIALS AND METHODS

A detailed procedure for the synthesis of the In_2O_3 is given in our recent publication (Aper et al., 2021). In brief, In_2O_3 nanostructures were prepared on nickel-coated silicon (Ni/Si) substrates using a mixture of

analytical In_2O_3 powder and graphite (in 1:1 mass ratio) as a precursor, pure nitrogen (N_2) gas as purging gas, 1 % hydrogen balance nitrogen (H_2/N_2) was used as forming/carrier gas. The temperature of the furnace was ramped from room temperature to 950 ºC in 30 min under 1000 sccm flow of N_2 gas. After reaching the set temperature, a mass of the precursor was taken in a ceramic boat and positioned in the central heating zone of the furnace. The substrate was placed horizontally on the back of a ceramic boat at a distance 25 cm downstream from the source material. The N_2 gas was then turned off, while 100 sccm of the H_2/N_2 was flown in through a vapor reservoir containing deionized water that was held at 70 ºC in the upstream direction. The deposition was carried out for 60 min after which the system was switched off and allowed to cool down in 30 min under a continuous flow of 400 sccm N_2 before removing the sample. Three other samples were deposited at H_2/N_2 flow rates of 150, 200, and 250 sccm, while keeping the other parameters constant to investigate the influence of gas flow rate on the materials' properties. The synthesized films were characterized for morphology using FEI Nova NanoSEM 450 field emission scanning electron microscope (FE-SEM), while the elemental composition was determined by energy dispersive X-ray (EDX) spectroscopy attached to the FESEM. Structural and optical properties were investigated using PANanalytical X' pert PRO high-resolution X-ray diffraction (HR-XRD) instrument with Cu K_α (λ=0.15406 nm) radiation source and ultraviolet-visible near-infrared spectrophotometer (UV-vis-NIR) Agilent Cary 5000 instruments, respectively.

RESULTS AND DISCUSSION

Surface morphology and elemental composition

The surface morphology for the In_2O_3 nanostructures as obtained from the FESEM measurement is given in Figure 1. The surface images revealed the formation of high-yield densely packed material in all the films. Hilly structures with multi-crystalline facets, truncated pyramids, and octahedrals, with some particulates scattered on their facets, can be observed in sample IO(100). For the growth under 150 sccm gas flow (sample IO(150)), a drastic reduction in the nanostructures' size and the number of surface particulates is observed. The structures are mainly consisting of incomplete pyramids and octahedral shapes. Nanochipping-like structures can be seen in sample IO(200). The size of the structures is also observed to be increased compared to those of IO(150). The surface particulates are completely eliminated in this sample. Faceted hilly structures with an increased size comparable to sample IO(100) can be observed in sample IO(250). The observed shape and size transformation in the material could be attributed to variations in the gas flow rates. A similar effect is also reported by Karn et al. (Karn et al., 2017).

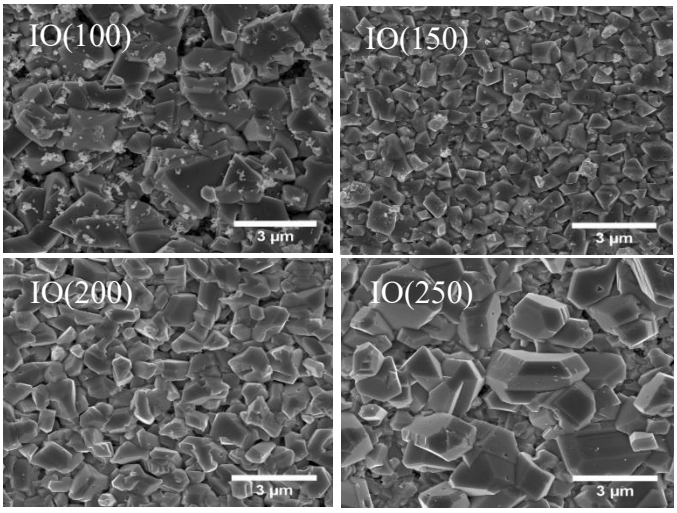

Figure 1: FESEM images of In_2O_3 nanostructures synthesized on Ni/Si at 950 ºC under various gas flow rates.

EDX measurement confirmed the elemental composition of the films to be mainly In and O in good proportion. A small percentage of Si due to the material of the substrates could also be seen for samples IO(100) and IO(150) that are synthesized under lower gas flow rates. The spectrograph for the samples' EDX is given in Figure 2, while the plot of In/O atomic ratio versus gas flow rate is presented in Figure 3. All the films are observed to be highly non-stoichiometric, with In/O values in the range of 1.56-1.74 above the stoichiometric value of 0.667. This is expected, as is usually the case with CVD synthesized films, due to oxygen deficiency in the

reaction chamber. It can also be related to the flow of H_2 gas, which may have contributed to the reducing effect. The In/O ratio is seen to increase with an increased gas flow rate as may be seen in Figure 3.

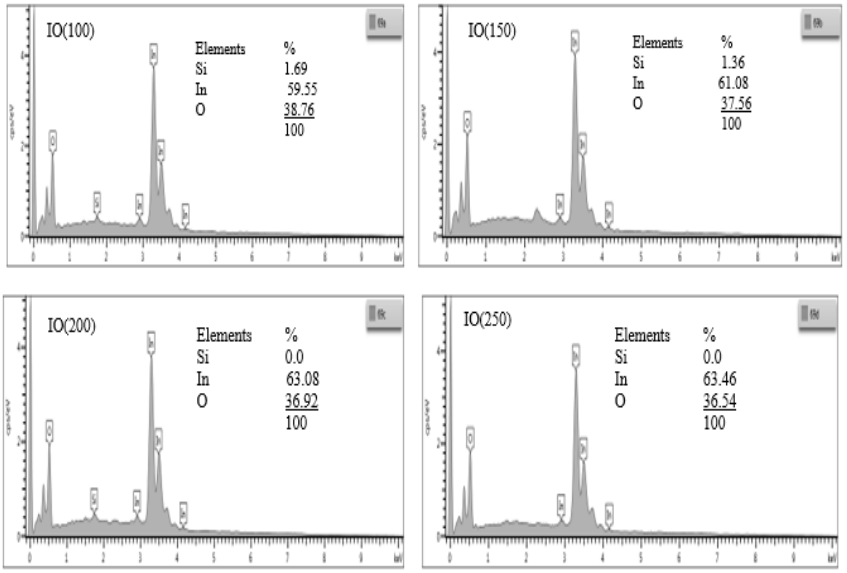

Figure 2: EDX spectrograph for In_2O_3 along with elemental composition films synthesis on Ni/Si under different gas flow rates

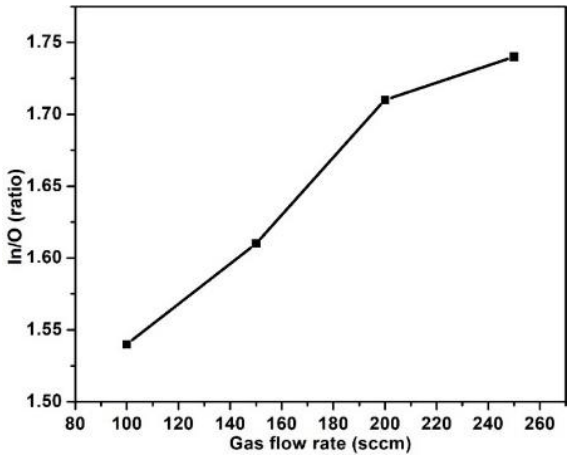

Figure 3: Variation of In/O atomic ratio with gas flow rate for In_2O_3 films prepared under different gas flow rates

Structural analysis

The phase and crystallinity of the samples were examined by XRD measurement. Figure 4(a) represents the diffractograms of the In_2O_3 nanostructured films. Various diffraction peaks attributed to the (211), (222), (400), (411), (332), (431), (440), (611), (622), (631), and (444) crystallographic planes of the bixbyite crystal structure of the In_2O_3 (JCPD card No. 00-044-1087). The absence of impurity peaks reveals the complete formation of In_2O_3 films. Judging by the high intensity of the (222) diffraction peak in all the samples implies that the In_2O_3 nanostructures exhibit preferential growth in the (222) plane. The relative intensity of the diffraction peaks is first observed to decrease with increased gas flow rate and increase with a further increase in gas flow rate. This could be ascribed to the nanostructures' particle size variations as revealed by the FESEM images.

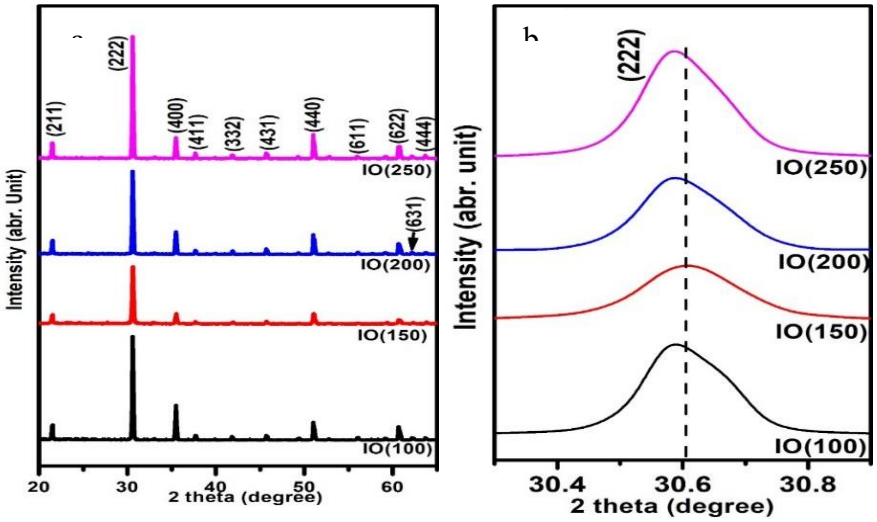

Figure 4: (a) XRD pattern, and (b) Zoom view of the most intense peak for the In_2O_3 films synthesized on Ni/Si at 950 °C under different gas flow rates.

The standard 2θ value for the (222) plane is 30.581 °, peak profile analysis from the most intense peak of the samples, however, shows a shift in the (222) peak position to larger angles for samples IO(100) and IO(150) synthesized respectively at 100 and 150 sccm gas flow rates. In contrast, for IO(200) and IO(250) synthesized at higher flow rates, the diffraction peaks shift to lower angles compared to the formal. It can also be observed in the zoom view of the dominant peak for samples Figure 4(b). Right shift or left shift in peak position could be attributed to strain due to lattice distortions arising from variations in the growth ambient. Structural parameters from the most intense peak of the samples were also estimated. The average grain size (D) and interplanar separation (d) were approximated using Eq. (1) and (2), respectively, while the lattice constants were estimated from the hkl value. Eq. (3) and (4) were used to calculate the strain (ε) and dislocation density (δ) in the samples, and percentage contraction was estimated from relation $d_{net} = ((d_{cal} - d_{ref})/d_{ref}) \times 100$. The estimated parameters are presented in Table 1 below.

$$D = \frac{0.9\lambda}{\rho \cos\theta} \quad (1)$$

$$n\lambda = 2d \sin\theta \quad (2)$$

$$\varepsilon = \frac{\beta \cos\theta}{4} \quad (3)$$

$$\delta = \frac{1}{D^2} \quad (4)$$

where λ=0.15406 nm is the wavelength of the XRD radiating source, ρ (radians) is the full width at half maximum (FWHM) (in radians) of the diffraction peak, θ (radians) is the Bragg's diffraction angle, and n=1 is the first diffraction order (Bindu & Thomas, 2014; Saw et al., 2015).

Table 1: Estimated structural parameters for In_2O_3 nanostructures grown on Ni/Si substrates at 950 °C, and various gas flow rates

Sample	2θ(°) (ref)	2θ(°) (obs)	d_{cal} (Å)	a (Å)	εx10^{-3}	δx10^{-3} (line/nm^2)	d(net) (%)
IO(100)		30.603	2.919	10.112	2.31	0.31	-0.071
IO(150)		30.611	2.918	10.109	2.81	0.46	-0.096
IO(200)	30.581	30.600	2.919	10.112	2.42	0.34	-0.061
IO(250)		30.598	2.919	10.131	2.23	0.29	-0.055

It can be observed from Table 1 that the measured 2θ for all the samples have shifted to the right as compared to the reference. It can also be observed that 2θ first increased with an increase in the gas flow and then decreased with a further increase in the gas flow rate. The shift to higher angles of 2θ for the In_2O_3 films grown under different gas flow rates is an indication that the crystalline cell experienced compressive stress. This is further confirmed as the d-spacing values of the samples are observed to be slightly less than the standard value of 2.921 and, the contraction in the interplanar distance (d(net)) are all negative (Yahia et al., 2019). The dependence of FWHM and crystallite size of the In_2O_3 on the gas flow rate is given in Figure 5. The plot shows an inverse relation between FWHM and crystallite size with an increased gas flow rate.

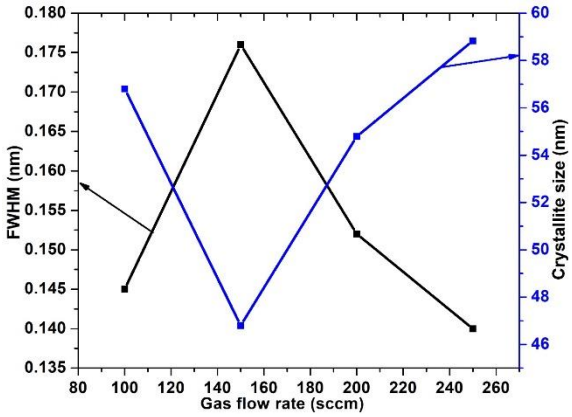

Figure 5: Variation of FWHM and crystallite size with a gas flow rate of In_2O_3 films synthesized under different gas flow rates

Optical characterization

The optical bandgap of the films was examined using the diffuse reflectance measurements in the spectral region $250 = \lambda = 800$nm. Using Kubalka-Munt (K-M) relation Eq. (5), the diffuse reflectance data was converted into absorbance to estimate the optical bandgap. Plots of diffuse reflectance (%) versus incident wavelength for the samples are given in Figure 6. As shown in Figure 6, all the films showed low reflectance of less than 10 %. A sharp absorption edge can be observed for sample IO(100) and IO(250). This may be ascribed to the large grain size and faceted nature of the films' structures. However, samples IO(150) and IO(200) with smaller grain sizes exhibit a shallow absorption edge.

$$F(R) = (1-R)^2/2R = \alpha/S \quad (5)$$

where $F(R)$is the K-M function, corresponding to the absorbance, $R$is the diffuse reflectance, α is the absorption coefficient, and $S$is the scattering coefficient, respectively (Džimbeg-Malčić et al., 2011).

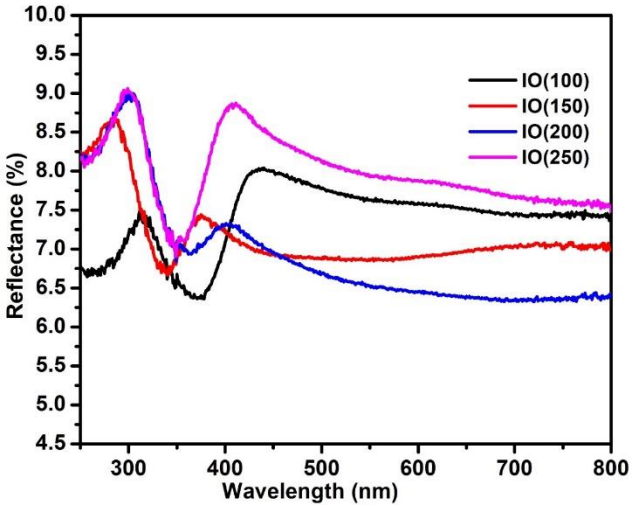

Figure 6: Diffuse reflectance (%) versus incident wavelength for the In_2O_3 films synthesized on Ni/Si at 950 ^oC under different gas flow rates

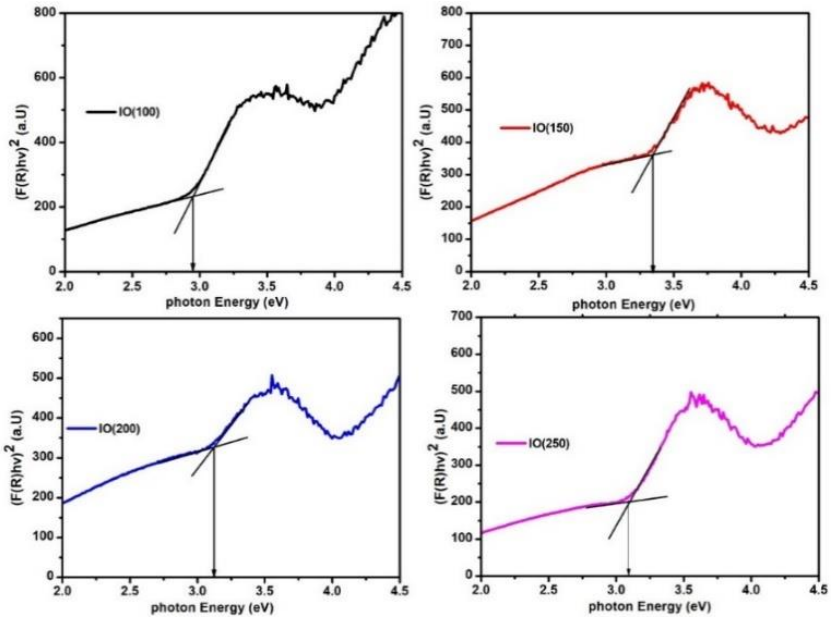

Figure 7: Plots of $(F(R)hv)^2$ versus incident photon energy for the In_2O_3 films synthesized on Ni/Si at 950 °C under different gas flow rates

Assuming the parabolic nature of the density of state for the conduction and the valence bands, Tauc's theory Eq. (6) was used alongside the K-M relation to approximate the optical bandgap of the coatings (Girtan & Folcher, 2003). Figure 7 represents the plots of $(F(R)hv)^2$ versus incident photon energy which gives E_g for the samples following proper extrapolation (Lotus et al., 2010; Makuła et al., 2018; Samanta et al., 2017). The bandgap values were first observed to increase with increased gas flow rate and decrease with further increase in gas flow rates. Usually, E_g of oxygen-deficient films is expected to decrease with increasing oxygen deficiency. However, the variations in the E_g values here do not seem to be totally dependent on the oxygen content of the films. Other factors, such as crystallite size and shape, may have played a dominant role in the observed E_g values. Figure 8 shows the variation of E_g and crystallite size versus gas flow rate. An inverse relation between E_g and crystallite size can readily be seen in Figure 8.

$$(\alpha hv) = A(hv - E_g)^n \quad (6)$$

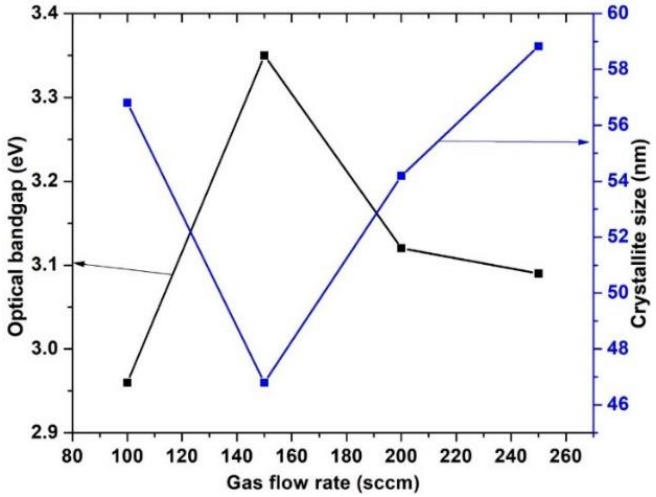

Figure 8: Variation of E_g, and crystallite size with gas flow rate for the In_2O_3 films synthesized on Ni/Si at 950 °C under different gas flow rates

CONCLUSION

Indium oxide nanostructured films were synthesized using the carbothermal reduction technique under atmospheric pressure. The prepared films' morphological, crystallographic, and optical properties were evaluated as a function of carrier gas flow rate. The result reveals a high density of material growth with changes in the nanostructure's shape and size with a variation in gas flow rates. The films were highly crystalline with preferential growth in the (222) plane of the cubic crystal structure of In_2O_3. XRD analysis reveals a complex variation in the crystallite size with gas flow rates. The optical bandgap was also observed to be inversely proportional to the grain size. The result demonstrates that using 1 % hydrogen balance nitrogen as a carrier gas in the CVD synthesis of indium oxide films is a possible way of varying the materials' properties for future potential applications.

ACKNOWLEDGMENT

Aper sincerely appreciates the School of Physics, Universiti Sains, Malaysia for providing all of the laboratory facilities for this research. The authors thank Rev. Fr. Moses Orshio Adasu University, (formally, Benue State University), Makurdi, Nigeria for providing an enabling environment.

REFERENCES

Abdulkadir, A., Abdul Aziz, A., & Pakhuruddin, M. Z. (2020). Properties of indium tin oxide on black silicon after post-deposition annealing for heterojunction solar cells. *Results in Physics*, *19*, 103405. https://doi.org/10.1016/j.rinp.2020.103405

Ahmed, N. M., Sabah, F. A., Abdulgafour, H. I., Alsadig, A., Sulieman, A., & Alkhoaryef, M. (2019). The effect of post annealing temperature on grain size of indium-tin-oxide for optical and electrical properties improvement. *Results in Physics*, *13*(February), 102159. https://doi.org/10.1016/j.rinp.2019.102159

Aper, T. M., Yam, F. K., & Beh, K. P. (2021). Materials Science in Semiconductor Processing Influence of temperature and nickel catalyst on the structural and optical properties of indium oxide nanostructured films synthesized by chemical vapor deposition technique. *Materials Science in Semiconductor Processing*, *132*(April), 105925. https://doi.org/10.1016/j.mssp.2021.105925

Bel, R., Tahar, H., Ban, T., Ohya, Y., Takahashi, Y., Bel, R., Tahar, H., Ban, T., Ohya, Y., & Takahashi, Y. (1998). *Electronic transport in tin-doped indium oxide thin films prepared by sol-gel technique Electronic transport in tin-doped indium oxide thin films prepared by sol-gel technique*. *2139*, 126–129. https://doi.org/10.1063/1.366949

Bindu, P., & Thomas, S. (2014). Estimation of lattice strain in ZnO nanoparticles: X-ray peak profile analysis. *Journal of Theoretical and Applied Physics*, *8*(4), 123–134. https://doi.org/10.1007/s40094-014-0141-9

Chen, Y., Yang, S., Lu, K., & Aesar, A. (2020). *Synthesis of High-Density Indium Oxide Nanowires with Low Electrical Resistivity*. 1–7.

Cho, J.-S., Koh, S.-K., & Yoon, K. H. (2000). Microstructure and Electrical Properties of Indium Oxide Thin Films Prepared by Direct Oxygen Ion-Assisted Deposition. *Journal of The Electrochemical Society*, *147*(3), 1065. https://doi.org/10.1149/1.1393314

Chong, S. K., Azizan, S. N. A., Chan, K. W., Nguyen, H. Q., Chiu, W. S., Aspanut, Z., Dee, C. F., & Rahman, S. A. (2013). Structure deformation of indium oxide from nanoparticles into nanostructured polycrystalline films by in situ thermal radiation treatment. *Nanoscale Research Letters*, *8*(1), 1–9. https://doi.org/10.1186/1556-276X-8-428

Džimbeg-Malčić, V., Barbarić-Mikočević, Ž., & Itrić, K. (2011). Kubelka-Munk theory in describing optical properties of paper (I). *Tehnički Vjesnik : Znanstveno-Stručni Časopis Tehničkih Fakulteta Sveučilišta u Osijeku*, *18*(1), 117–124.

Elam, J. W., Martinson, A. B. F., Pellin, M. J., & Hupp, J. T. (2006). Atomic layer deposition of in 2O 3 using cyclopentadienyl indium: A new synthetic route to transparent conducting oxide films. *Chemistry of Materials*, *18*(15), 3571–3578. https://doi.org/10.1021/cm060754y

Girtan, M., & Folcher, G. (2003). Structural and optical properties of indium oxide thin films prepared by an ultrasonic spray CVD process. *Surface and Coatings Technology*, *172*(2–3), 242–250. https://doi.org/10.1016/S0257-8972(03)00334-7

Hassanien, A. S., & Akl, A. A. (2016). Effect of Se addition on optical and electrical properties of chalcogenide CdSSe thin films. *Superlattices and Microstructures*, *89*(January), 153–169. https://doi.org/10.1016/j.spmi.2015.10.044

Her, S. C., & Chang, C. F. (2017). Fabrication and characterization of indium tin oxide films. *Journal of Applied Biomaterials and Functional Materials*, *15*(2), e170–e175. https://doi.org/10.5301/jabfm.5000345

Hoch, L. B., O'Brien, P. G., Jelle, A., Sandhel, A., Perovic, D. D., Mims, C. A., & Ozin, G. A. (2016). Nanostructured Indium Oxide Coated Silicon Nanowire Arrays: A Hybrid Photothermal/Photochemical Approach to Solar Fuels. *ACS Nano*, *10*(9), 9017–9025. https://doi.org/10.1021/acsnano.6b05416

Hosseini, a, Icli, K. C., & Güllü, H. H. (2013). Preparation and characterization of porous TiO 2 thin films by sol-gel method for Extremely Thin Absorber-ETA solar cell applications Çok ince Soğurucu – ETA g üneş gö zeler e uygulamaları için gö zenekli TiO 2 ince filmlerin sol-jel metodu ile ü retilmes. *Turkish Journal of Science & Technology*, *8*(2), 69–79.

Karn, A., Kumar, N., & Aravindan, S. (2017). Chemical vapor deposition synthesis of novel indium oxide nanostructures in strongly reducing growth ambient. *Journal of Nanostructures*, *7*(1), 64–76. https://doi.org/10.22052/jns.2017.01.008

King, P. D. C., Veal, T. D., Fuchs, F., Wang, C. Y., Payne, D. J., Bourlange, A., Zhang, H., Bell, G. R., Cimalla, V., Ambacher, O., Egdell, R. G., Bechstedt, F., & McConville, C. F. (2009). Band gap, electronic structure, and surface electron accumulation of cubic and rhombohedral In2 O3. *Physical Review B - Condensed Matter and Materials Physics*, *79*(20), 1–10. https://doi.org/10.1103/PhysRevB.79.205211

Lotus, A. F., Feaver, R. K., Britton, L. A., Bender, E. T., Perhay, D. A., Stojilovic, N., Ramsier, R. D., & Chase, G. G. (2010). Characterization of TiO2-Al2O3 composite fibers formed by electrospinning a sol-gel and polymer mixture. *Materials Science and Engineering B: Solid-State Materials for Advanced Technology*, *167*(1), 55–59. https://doi.org/10.1016/j.mseb.2010.01.027

Makhija, K. K., Ray, A., Patel, R. M., Trivedi, U. B., & Kapse, H. N. (2005). Indium oxide thin film based ammonia gas and ethanol vapour sensor. *Bulletin of Materials Science*, *28*(1), 9–17. https://doi.org/10.1007/BF02711165

Makuła, P., Pacia, M., & Macyk, W. (2018). How To Correctly Determine the Band Gap Energy of Modified Semiconductor Photocatalysts Based on UV-Vis Spectra. *Journal of Physical Chemistry Letters*, *9*(23), 6814–6817. https://doi.org/10.1021/acs.jpclett.8b02892

Prathap, P., Subbaiah, Y. P. V, Devika, M., & Reddy, K. T. R. (2005). *Investigations on the Structural Properties of Sprayed In 2 O 3 Films*. 1021–1022.

Qurashi, A., Irfan, M. F., & Alam, M. W. (2010). In2O3 nanostructures and their chemical and biosensor applications. *Arabian Journal for Science and Engineering*, *35*(1 C), 125–145.

Samanta, B., Dutta, D., & Ghosh, S. (2017). Synthesis and different optical properties of Gd2O3 doped sodium zinc tellurite glasses. *Physica B: Condensed Matter*, *515*(June 2016), 82–88. https://doi.org/10.1016/j.physb.2017.03.036

Saw, K. G., Aznan, N. M., Yam, F. K., Ng, S. S., & Pung, S. Y. (2015). New insights on the burstein-moss shift and band gap narrowing in indium-doped zinc oxide thin films. *PLoS ONE*, *10*(10), 1–17. https://doi.org/10.1371/journal.pone.0141180

Tuzluca, F. N., Yesilbag, Y. O., & Ertugrul, M. (2018). Synthesis of In 2 O 3 nanostructures with different morphologies as potential supercapacitor electrode materials. *Applied Surface Science*, *427*, 956–964. https://doi.org/10.1016/j.apsusc.2017.08.127

Yahia, A., Attaf, A., Saidi, H., Dahnoun, M., Khelifi, C., Bouhdjer, A., Saadi, A., & Ezzaouia, H. (2019). Structural, optical, morphological and electrical properties of indium oxide thin films prepared by sol gel spin coating process. *Surfaces and Interfaces*, *14*(October 2018), 158–165. https://doi.org/10.1016/j.surfin.2018.12.012